

# We are IntechOpen, the world's leading publisher of Open Access books Built by scientists, for scientists

4,800

Open access books available

122,000

International authors and editors

135M

Downloads

Our authors are among the

154

Countries delivered to

TOP 1%

most cited scientists

12.2%

Contributors from top 500 universities



WEB OF SCIENCE™

Selection of our books indexed in the Book Citation Index  
in Web of Science™ Core Collection (BKCI)

Interested in publishing with us?  
Contact [book.department@intechopen.com](mailto:book.department@intechopen.com)

Numbers displayed above are based on latest data collected.  
For more information visit [www.intechopen.com](http://www.intechopen.com)



# Biomedical Image Segmentation Based on Multiple Image Features

Jinhua Yu<sup>1,2</sup>, Jinglu Tan<sup>1</sup> and Yuanyuan Wang<sup>2</sup>

<sup>1</sup>*University of Missouri*

<sup>2</sup>*Fudan University*

<sup>1</sup>*USA*

<sup>2</sup>*China*

## 1. Introduction

Image segmentation is a procedure that partitions an image into disjointing segments with each segment sharing similar properties such as intensity, color, boundary and texture. In general, three main types of image features are used to guide image segmentation, which are intensity or color, edge, and texture. In other words, image segmentation methods generally fall into three main categories: intensity-based (or color-based), edge-based, and texture-based segmentations.

Intensity-based segmentation assumes that an image is composed of several objects with constant intensity. This kind of methods usually depends on intensity similarity comparisons to separate different objects. Histogram thresholding (Otsu, 1979; Sahoo et al., 1988), clustering (Bezdek, 1981; Pappas, 1992), and split-and-merge (Tyagi & Bayoumi, 1992; Wu, 1993) are examples of intensity-based segmentation methods.

Edge-based segmentation has a strong relationship with intensity-based segmentation, since edges usually indicate discontinuities in image intensity. Edge-based segmentation uses different methods to describe the salient edges in images. Then, the boundaries of objects are detected by edge grouping or edge-driven active contour construction. Widely-used methods in edge-based segmentation include Canny (Canny 1986), watershed (Vincent & Soille, 1991) and snake (Kass et al., 1998; Xu & Prince, 1998).

Texture is another important characteristic used to segment objects in an image. Most texture-based segmentation algorithms map an image into a texture feature space, then statistical classification methods (Randen & Husoy, 1999) are usually used to differentiate texture features. Co-occurrence matrix (Zucker & Terzopoulos, 1980), directional gray-level energy (Hsiao & Sawchuk, 1989), Gabor filters (Jain & Farrokhnia, 1991), and fractal dimension (Mandelbrot, 1976; Pentland 1984) are frequently used methods to obtain texture features.

Biomedical images usually suffer from certain imaging artifacts stemming from different imaging modalities. Because of imperfect illumination, signal attenuation or signal superposition in biomedical images, intensity-based segmentation methods are often ineffective in differentiating neighboring tissues with similar intensity features. Further, because of noises in biomedical images, detected tissue edges are often discontinuous, obstructed, or obscure. It remains a problem in edge-based segmentation to interpret and connect discontinuous edges. As a high-level image characteristic, texture reflects the spatial

arrangement of intensity, color or shape. Texture features could be easily spoiled by imperfect imaging conditions mentioned above. As a result, a single image feature is usually not sufficient to produce satisfactory segmentation for biomedical images. Multiple image features can be combined to enhance segmentation. This chapter provides three applications illustrating how multiple image features are integrated for segmentation of images generated from different modalities.

2. Fetal abdominal contour measurement in ultrasound images

Because of its noninvasiveness, ultrasound imaging is the most prevalent diagnostic technique used in obstetrics. Fetal abdominal circumference (AC), an indicator of fetal growth, is one of the standardized measurements in antepartum ultrasound monitoring. In the first application, a method that makes effective use of the intensity and edge information is provided to outline and measure the fetal abdominal circumference from ultrasound images (Yu et al., 2008a; Yu et al., 2008b).

2.1 Algorithm overview

Fig. 1 summarizes the segmentation algorithm for abdomen measurement.

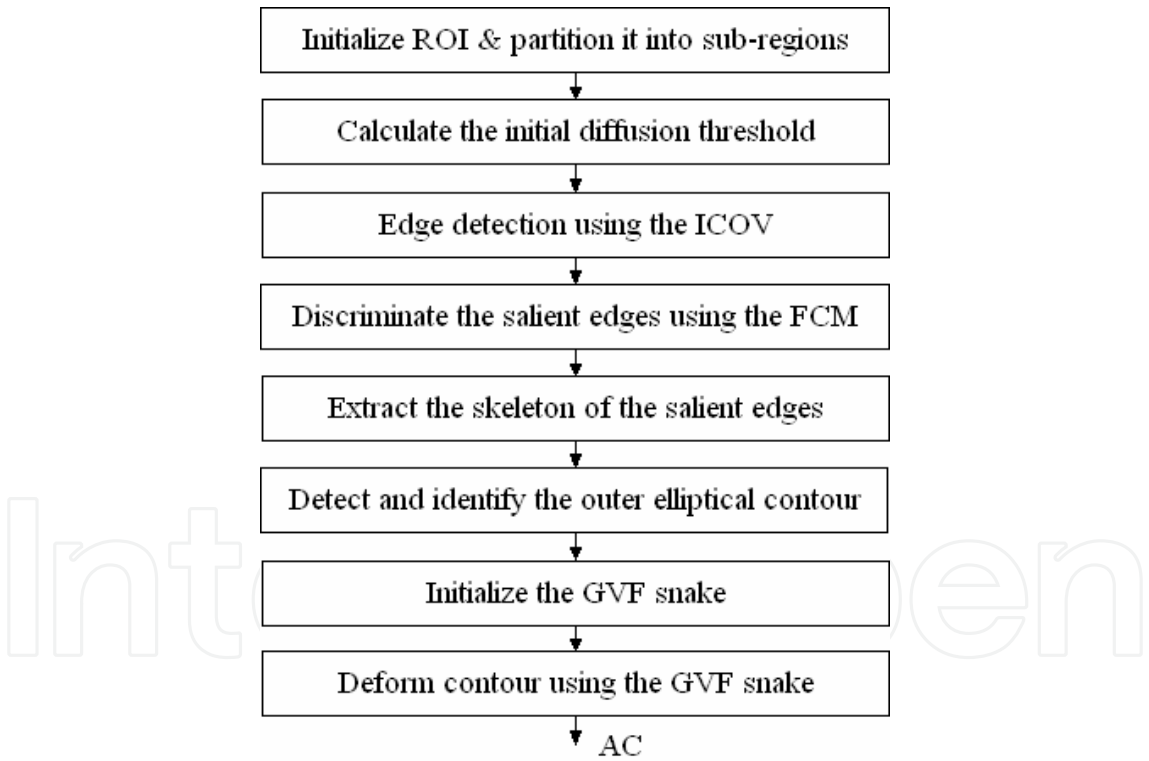


Fig. 1. Flowchart of segmentation algorithm for abdomen measurement.

In the first step, a rectangle enclosing the contour of the target object, is given by the operator (as shown in Fig. 2(a)), then a region of interest (ROI) is defined in the form of an elliptical ring within the manually defined rectangle. The outer ellipse of the ring inscribes the rectangle. The inner ellipse is 30% smaller than the outer ellipse. To accommodate edge strength variations, the ROI is equally partitioned into eight sub-regions. In the second step, the initial diffusion threshold is calculated for each sub-region. Instantaneous coefficient of

variation (ICOV) is used to detect the edges of the abdominal contour in the third step. The detected edges are shown in Fig. 2(b). The fuzzy C-Means (FCM) clustering algorithm is then used to distinguish between salient edges of the abdominal contour and weak edges resulting from other textures. Salient edges are then thinned to serve as the input to the next step. As shown in Fig. 2 (c), bright pixels are the salient edges, and dark lines within the bright pixels are the skeleton of the edges. In the sixth step, randomized Hough transforms (RHT) is used to detect and locate the outer contour of AC. The detected ellipse for AC is shown in Fig. 2 (d). To improve AC contour extraction in the seventh and eighth steps, a GVF snake is employed to adapt the detected ellipse to the real edges of the abdominal contour. The final segmentation by the GVF snake is shown in Fig. 2(e). For comparison, the original ROI image and the manual AC contour are shown in Fig. 2(f) and 2(g), respectively.

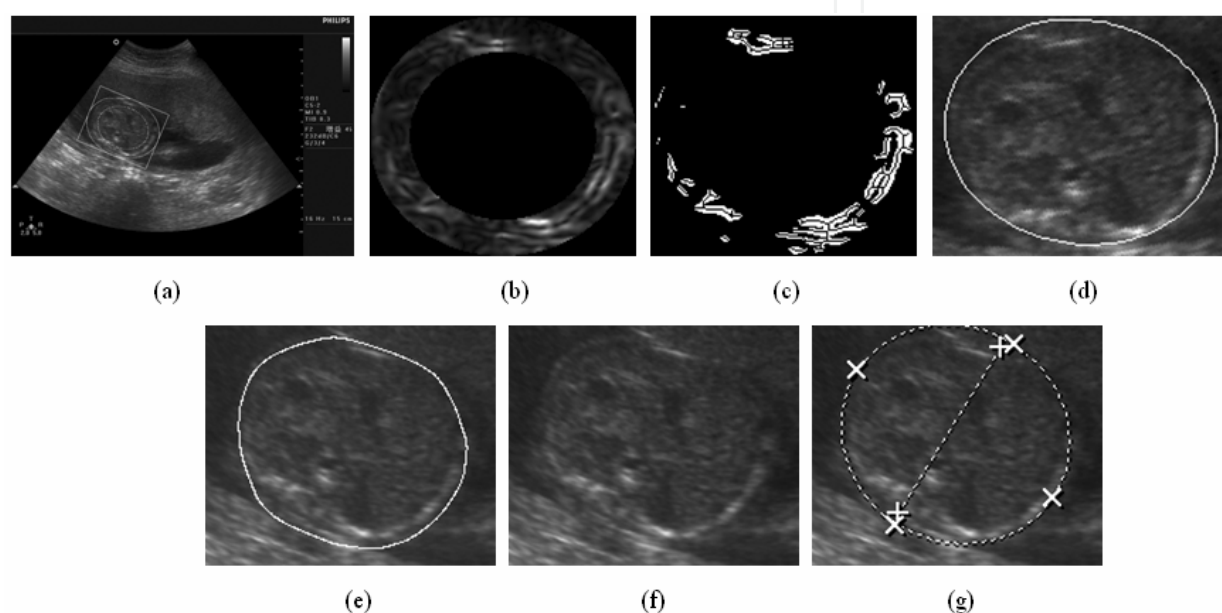


Fig. 2. Segmentation and measurement of fetal abdomen. (a) ROI definition, (b) Edge map detected by ICOV, (c) Salient edges with skeleton, (d) Initial contour obtained by RHT, (e) Final abdominal contour, (f) Original image, (g) Manually extracted abdominal contour.

## 2.2 Edge detection of the abdominal contour

For images that contain strong artifacts, it is difficult to detect boundaries of different tissues without being affected by noise. A regular edge detector such as Canny operator (Canny, 1986), Haralick operator (Haralick 1982) or Laplacian - of - Gaussian operator (FjØrtoft et al., 1998) can not provide satisfactory results. The instantaneous coefficient of variation (ICOV) (Yu & Acton, 2004) provides improvement in edge-detection over traditional edge detectors. The ICOV edge-detection algorithm combines a partial differential equation-based speckle-reducing filter (Yu & Acton, 2002) and an edge strength measurement in filtered images. With the image intensity at the pixel position  $(x,y)$  denoted as  $I$ , the strength of the detected edge at time  $t$ , denoted as  $q(x,y;t)$ , is given by

$$q(x,y;t) = \sqrt{\frac{\left(\left(\frac{1}{2}\right)\|\nabla I\|^2 - \left(\frac{1}{16}\right)(\nabla^2 I)^2\right)}{\left(I + \left(\frac{1}{4}\right)\nabla^2 I\right)^2}} \quad (1)$$

where  $\nabla, \nabla^2, \|\cdot\|$ , and  $|\cdot|$  are the gradient, Laplacian, gradient magnitude, and absolute value, respectively. The speckle reduction is achieved via a diffusion process, which is determined by a diffusion coefficient defined as

$$c(q) = \frac{1}{1 + [q^2(x, y; t) - q_0^2(t)] / [q_0^2(t)(1 + q_0^2(t))]} \quad (2)$$

where  $q_0(t)$  is the diffusion threshold to determine whether to encourage or inhibit the diffusion process. The selection of an appropriate  $q_0(t)$  has paramount effects on the performance of speckle reduction hence the performance of edge detection. To be adaptive to edge strength variation, the ROI is equally partitioned into eight sub-regions. The initial diffusion threshold  $q_0$  for each sub-region is formulated as

$$q_0 = \frac{\sqrt{\text{var}[SR]}}{\overline{SR}} \quad (3)$$

where  $\text{var}[SR]$  and  $\overline{SR}$  are the intensity variance and mean of each sub-region SR.  $q_0(t)$  is approximated by  $q_0(t) = q_0 \exp[-t/6]$ , where  $t$  represents the discrete diffusion time step.

### 2.3 Edge map simplification

In order to distinguish between salient edges of the abdominal contour and weak edges from other textures, the fuzzy C-Means (FCM) clustering algorithm (Bezdek, 1980) is employed. Let  $X = \{I_1, I_2, \dots, I_n\}$  be a set of  $n$  data points, and  $c$  be the total number of clusters or classes. The objective function for partitioning  $X$  into  $c$  clusters is given by

$$J_{FCM} = \sum_{j=1}^c \sum_{i=1}^n \mu_{ij}^2 \|I_i - m_j\|^2 \quad (4)$$

where  $m_j, j=1, 2, \dots, c$  represent the cluster prototypes and  $\mu_{ij}$  gives the membership of pixel  $I_i$  in the  $j$ th cluster  $m_j$ . The fuzzy partition matrix satisfies

$$U = \left\{ \mu_{ij} \in [0, 1] \mid \sum_{j=1}^c \mu_{ij} = 1 \quad \forall i \quad \text{and} \quad 0 < \sum_{i=1}^N \mu_{ij} < N \quad \forall j \right\} \quad (5)$$

Under the constraint of (5), setting the first derivatives of (4) with respect to  $\mu_{ij}$  and  $m_j$  to zero yields the necessary conditions for (4) to be minimized. Based on the edge strength, each pixel in the edge map is classified into one of three clusters: salient edges, weak edges, and the background. Then salient edges (bright pixels in Fig. 2(c)) are thinned (dark curves in Fig. 2(c)) to serve as the input to the next step.

### 2.4 Initial abdominal contour estimation & contour deformation

Randomized Hough transform (RHT) depends on random sampling and many-to-one mapping from the image space to the parameter space in order to achieve effective object detection. An iterative randomized Hough transform (IRHT) (Lu et al., 2005), which applies the RHT to an adaptive ROI iteratively, is used to detect and locate the outer contour of AC. A parametric representation of ellipse is:

$$a_1x^2 + a_2xy + a_3y^2 + a_4x + a_5y + 1 = 0 \quad (6)$$

At the end of each round of the RHT, the skeleton image is updated by discarding the pixels within an ellipse which is 5% smaller than the detected ellipse. At the end of IRHT iterations, edges located on the outer boundary remain; and the detected ellipse converges to the outer contour of the abdomen.

The active contour model, or snake method as commonly known, is employed to find the best fit between the final contour and the actual shape of the AC. A snake is an energy-minimizing spline guided by external constraint forces computed from the image data and influenced by image forces coming from the curve itself (Kass et al., 1988). To overcome problems associated with initialization and poor convergence to boundary concavities of a classical snake, an new external force field called gradient vector flow (GVF) is introduced (Xu & Prince, 1998). The GVF field is defined as the vector field  $v(x, y)$  that minimizes the following energy functional

$$E = \iint \mu |\nabla \mathbf{v}|^2 + |\nabla f|^2 |\mathbf{v} - \nabla f|^2 dx dy \quad (7)$$

where  $\mu$  is a parameter governing the tradeoff between the first term and the second term in the integrand,  $\nabla$  is the gradient operator which is applied to each component of  $\mathbf{v}$  separately, and  $f$  represents the edge map. Fig. 2(e) shows the final segmentation by the GVF snake with the skeleton image as the object and the detected ellipse (Fig. 2(d)) as the initial contour.

## 2.5 Algorithm performance

Fig. 3 gives results of automatic abdominal contour estimation and manual delineation on four clinical ultrasound images. The four images represent some typical conditions that often occur in daily ultrasound measurements. The first row is for a relatively ideal ultrasound image of abdominal contour. There is plenty of amniotic fluid around the fetal body to give good contrast between the abdominal contour and other tissues. The second row represents a circumstance, in which one of fetal limbs superposed on the top left of the abdominal contour. The next row shows a case where the part of contour is absent as a result of shadow. Other circumstances may cause partial contour absence, such as signal dropout, improper detector positioning, or signal attenuation. The last row shows a case of contour deformation because of the pressure on the placenta. The first column to the third column show the original images, delineations by physicians, and the final contour by the GVF snake, respectively.

The method takes advantage of several image segmentation techniques. Experiments on clinical ultrasound images show that the accurate and consistent measurements can be obtained by using the method. The method also provides a useful framework for ultrasound object segmentation with a priori knowledge of the shape. Beside the fetal head, the vessel wall in the intravascular ultrasound, and the rectal wall in the endorectal ultrasound are other potential applications of the method.

## 3. Cell segmentation in pathological images

Pathological diagnosis often depends on visual assessment of a specimen under a microscope. Isolating the cells of interest is a crucial step for cytological analysis. For instance, separation of red and white pulps is important for evaluating the severity of tissue infections. Since lymphocyte nuclei are densely distributed in the white pulps, the nucleus



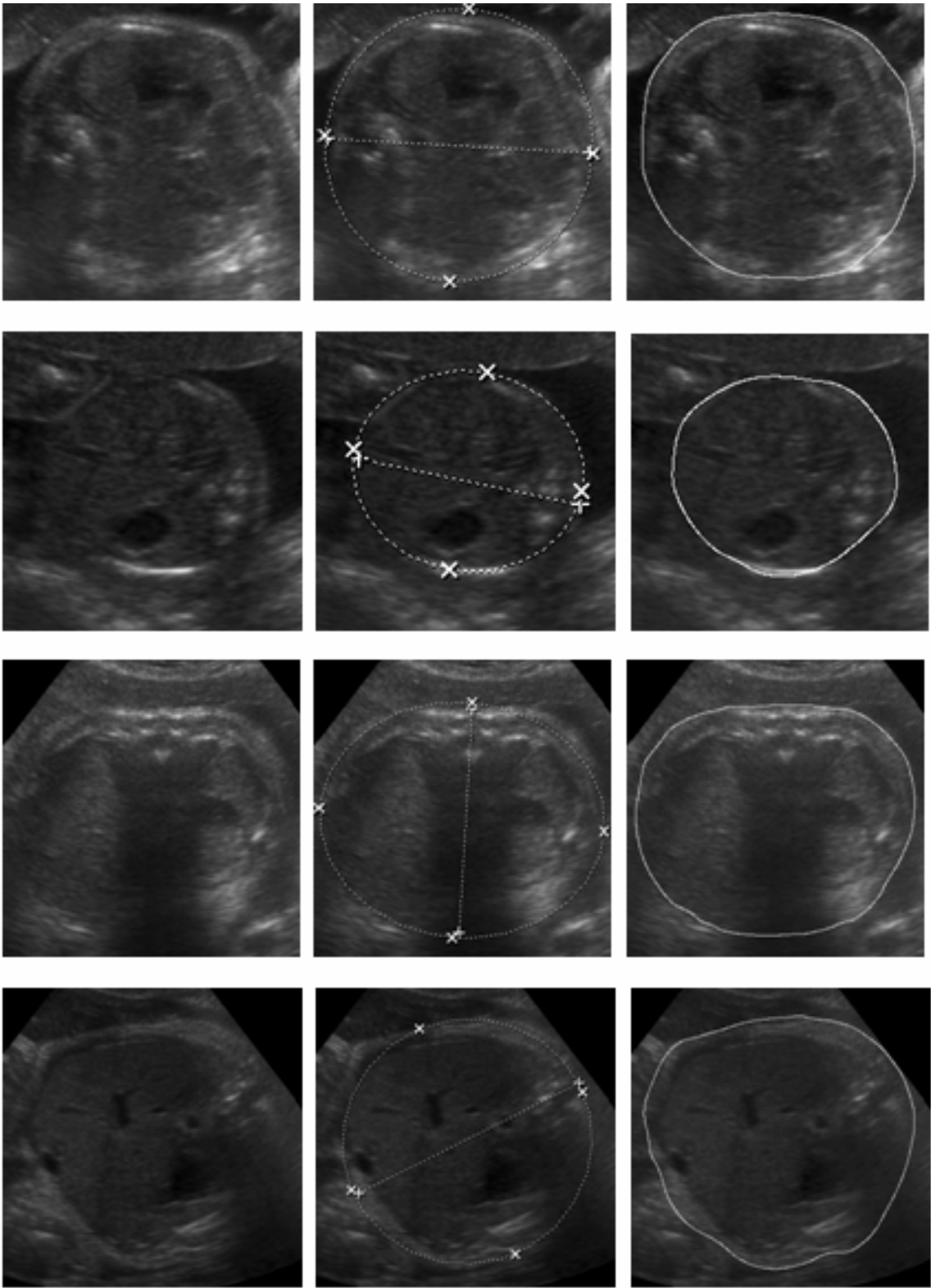


Fig. 3. Abdominal contour estimation on four clinical images. First column, from top to bottom: images represent relatively good, superposition interference, contour absence, and contour deformation, respectively. Second column: delineations by physicians. Third column: detected ellipses by the IRHT. Fourth column: final contours obtained by the GVF snake.

density serves as a segmentation criterion between red and white pulps. The second application demonstrates a cell segmentation method which incorporates intensity-based, edge-based and texture-based segmentation techniques (Yu & Tan, 2009).

3.1 Algorithm overview

Fig. 4 gives the flowchart of the cell segmentation algorithm. The algorithm first uses histogram adjustment and morphological operations to enhance a microscopic image, reduce noise and detect edges. Then FCM clustering is utilized to extract the layer of interest (LOI) from the image. Following preprocessing, conditional morphological erosion is used to mark individual objects. The marker-controlled watershed technique is subsequently employed to identify individual cells from the background. The main tasks of this stage are marker extraction and density estimation. The segmented cells are the starting point for the final stage, which then characterizes the cell distribution by textural energy. A textural energy-driven active contour algorithm is designed to outline the regions of desired object density. In the final stage, two important parameters are determined by the result of object segmentation, which are the window size for fractal dimension computation and the termination condition for the active contour algorithm.

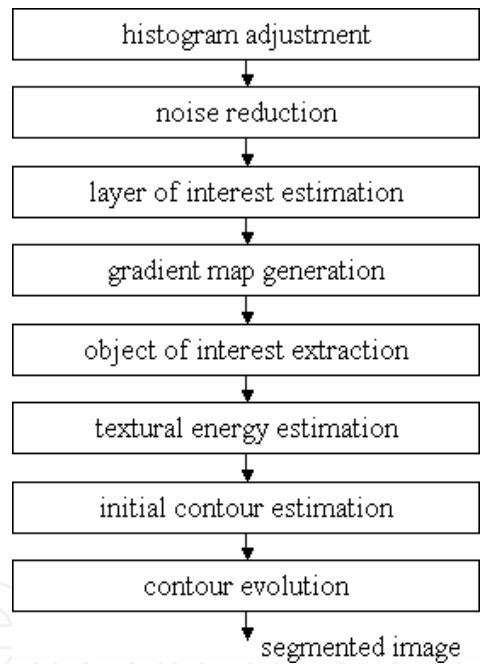


Fig. 4. Flowchart of the cell segmentation algorithm

3.2 Image preprocessing

The preprocessing stage consists of several subtasks including image enhancement, noise reduction, gradient magnitude estimation and preliminary LOI extraction. Fig. 5(a) shows an image of rat spleen tissue. The tissue section was stained with haematoxylin and eosin (H&E) for visual differentiation of cellular components. Under a microscope, nuclei are usually dark blue, red blood cells orange/red, and muscle fibers deep pink/red. The density of the lymphocytes is a key feature to differentiate red and white pulps. The white pulp has lymphocytes and macrophages surrounding central arterioles. The density of the lymphocytes in the red pulp is much lower than that in the white pulp. Evaluating the



severity of infection requires identifying the infected regions or the white pulp. To simplify the subsequent processing procedure, color images are transformed into gray level images. Histogram adjustment (Larson *et al.*, 1997) is used to widen the dynamic range of the image and increase the image contrast. Following image enhancement, grayscale morphological reconstruction (Vincent, 1993) is used to reduce noise and simplify image construction. Although morphological reconstruction can smooth slow intensity variations effectively, it is sensitive to sharp intensity variations, such as impulsive noise. Since median filtering can remove transient spikes easily and preserve image edges at the same time, it is applied to the image obtained from morphological reconstruction. Fig. 5(b) shows the output image after histogram adjustment, morphological reconstruction and median filtering. FCM is used to classify each pixel according to its intensity into  $c$  categories. Then the category with the high intensity is defined as LOI. Fig. 5(c) shows the LOI obtained from FCM clustering. A gradient magnitude image (Fig. 5(d)) is computed for subsequent use by a watershed algorithm.

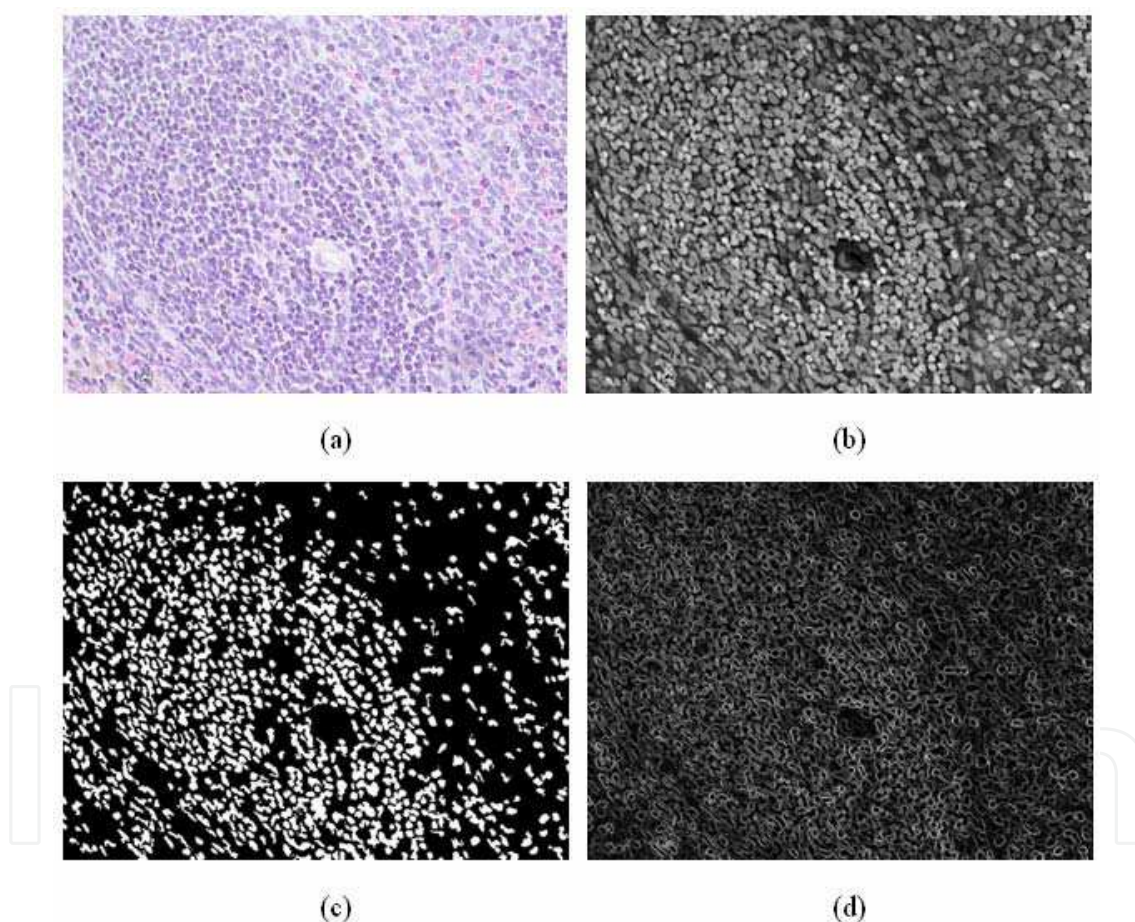


Fig. 5. Preprocessing of microscopic image. (a) Original image. (b) Image after histogram adjustment, morphological reconstruction and median filtering. (c) LOI obtained from FCM clustering. (d) Morphological gradient map.

### 3.3 Object segmentation

After the preprocessing stage, objects are extracted from the background. From Fig. 5(c), we can see that touching objects can not be separated by using FCM clustering, which will lead to errors in density estimation. Watershed (Vincent & Soille, 1991; Yang & Zhou, 2006) is known

to be an effective tool to deal with such a problem. Simulation of an immersion process is an efficient algorithm to compute the watershed line. The gradient magnitude image is used for watershed computation. The gradient is treated as a topographical map with the height of each point directly related to its gradient magnitude. The topography defined by the image gradient is flooded through holes pierced at the bottom of valley. The flooding progresses at constant rate from each hole upwards and the catchment basins containing the holes are flooded. At the point where waters would mix, a dam is built to avoid mixing waters coming from different catchment basins. Since each minimum of the gradient leads to a basin, the watershed algorithm usually produces too many image segments. Several techniques (Yang & Zhou, 2006; Hairs *et al.*, 1998; Jackway, 1996) have been proposed to alleviate this problem. Marker-controlled watershed is the most commonly used one, in which a marker image is used to indicate the desired minima of the image, thus predetermining the number and location of objects. A marker is a set of pixels within an object used to identify the object. The simplest markers can be obtained by extracting the regional minima of the gradient image. The number of regional minima could, however, be large because of the intensity fluctuations caused by noise or texture. Here, conditional erosion (Yang & Zhou, 2006) is used to extract markers. Fine and coarse erosion structures are conditionally chosen for erosion operations according to the shape of objects, and the erosions are only done when the size of the object is larger than a predefined threshold. The coarse and fine erosion structures utilized in this work are shown in Fig 6. Fig. 7(a) shows the marker map obtained and Fig. 7(b) gives segmented objects.

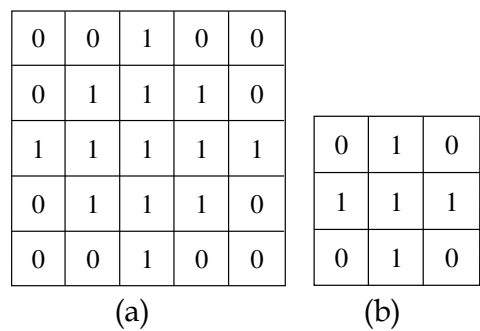


Fig. 6. Structuring element (SE). (a) Coarse SE. (b) Fine SE.

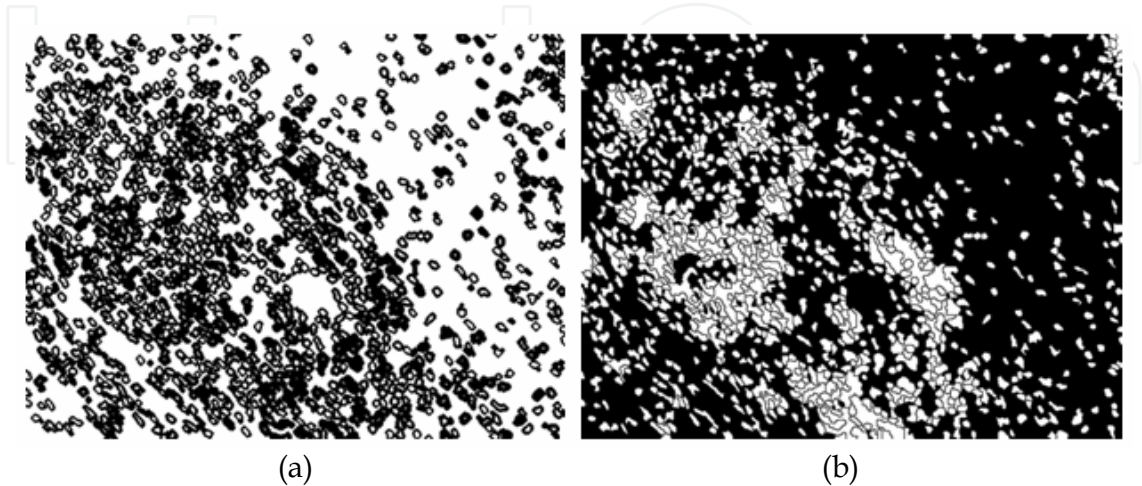


Fig. 7. Object segmentation. (a) Marker map. (b) OI segmentation by marker-controlled watershed.

### 3.4 Final segmentation

Many image features can be used to characterize the spatial density of objects. An object image may be characterized as an image texture. It has been long recognized that the fractal model of three-dimensional surfaces can be used to obtain shape information and to distinguish between smooth and rough textured regions (Pentland, 1984). In this application, fractal dimension is used to extract textural information from images. Several methods have been reported to measure the fractal dimension (FD). Among these methods, differential box-counting (DBC) (Chaudhuri & Sarkar, 1995) is an effective and commonly used approach to estimating fractal dimension of images.

Assume that an  $M \times M$  image has been partitioned into grids of size  $m \times m$ , where  $M/2 \geq m > 1$  and  $m$  is an integer. Then the scale ratio  $r$  equals to  $m/M$ . Consider the image as a three-dimensional (3D) surface, with  $(x, y)$  denoting 2D position and the third coordinate ( $z$ ) denoting the gray level of the corresponding pixel. Each grid contains  $m \times m$  pixels in the  $x$ - $y$  plane. From a 3D point of view, each grid can be represented as a column of boxes of size  $m \times m \times m'$ . If the total number of gray levels is  $G$ , then  $m' = \lceil r \times G \rceil$ .  $\lceil \cdot \rceil$  means rounding the value to the nearest integers greater than or equal to that value. Suppose that the grids are indexed by  $(i, j)$  in the  $x$ - $y$  plane, and the minimum and maximum gray levels of the image in the  $(i, j)$ th grid fall in the  $k$ th and the  $l$ th boxes in the  $z$  direction, respectively, then

$$n_{r(i,j)} = l - k + 1 \quad (8)$$

is the contribution of the  $(i, j)$ th grid to  $N_r$ , which is defined as:

$$N_r = \sum_{i,j} n_{r(i,j)} \quad (9)$$

$N_r$  is counted for different values of  $r$  (i.e., different values of  $m$ ). Then, the fractal dimension can be estimated as:

$$D = \frac{\log(N_r)}{\log(1/r)} \quad (10)$$

The FD map of an image is generated by calculating the FD value for each pixel. A local window, which is centered at each pixel, is used to compute the FD value for the pixel. Fig. 8(a) shows the textural energy map generated from fractal dimension analysis.

An active contour model is used to isolate the ROI based on the texture features. Active contour model-based algorithms, which progressively deform a contour toward the ROI boundary according to an objective function, are commonly-used and intensively-researched techniques for image segmentation. Active contour without edges is a different model for image segmentation based on curve evolution techniques (Chan & Vese, 2001). For the convenience of description, we refer to this model as the energy-driven active contour (EDAC) model for the fact that the textural energy will be used to control the contour deformation. The energy functional of the EDAC model is defined by

$$\begin{aligned} F(c_1, c_2, C) = & \mu \cdot \text{Length}(C) + \nu \cdot \text{Area}(\text{inside}(C)) \\ & + \lambda_1 \int_{\text{inside}(C)} |I_0(x, y) - c_1|^2 dx dy \\ & + \lambda_2 \int_{\text{outside}(C)} |I_0(x, y) - c_2|^2 dx dy \end{aligned} \quad (11)$$



where  $I_0(x, y)$  is the textural energy image,  $C$  is a variable contour, and  $c_1$  and  $c_2$  are the averages of  $I_0$  inside and outside  $C$ , respectively.  $\mu \geq 0$ ,  $\nu \geq 0$ ,  $\lambda_1, \lambda_2 > 0$  are weighting parameters.

To apply the EDAC model, an initial contour must be chosen. From the previous step, the FD-based texture feature map represents the textural energy distribution of OIs. FCM clustering is utilized to estimate the initial contour for EDAC. The active contour evolution starts from the region with the highest object intensity, which corresponds to the region with the highest textural energy. FCM is used to classify textural energy into  $c$  clusters, and the region corresponding to the cluster with the highest textural energy is chosen as the initial contour. Fig. 8(b) shows the final contour obtained from EDAC.

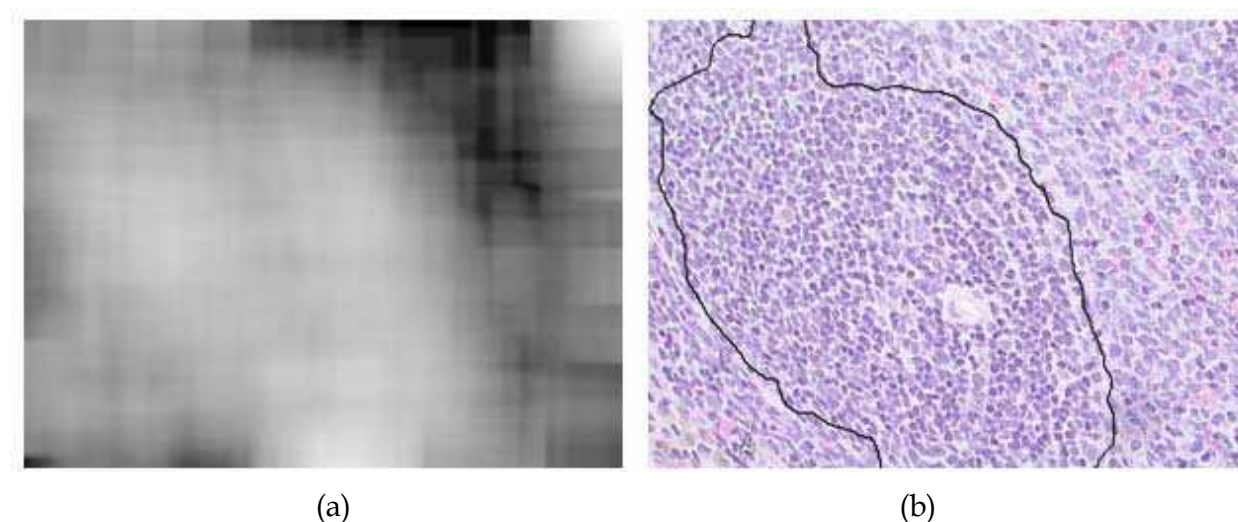


Fig. 8. Final segmentation. (a) Textural energy generated from fractal dimension analysis. (b) Initial contour. (c) Final segmentation obtained from EDAC.

### 3.5 Algorithm performance

Fig. 9(a) shows another microscopic spleen tissue image. Fig. 9(b) to (e) show the results of preprocessing, object segmentation, textural energy map computation, and final segmentation. From Fig. 9(b), it is clear that the noise is reduced and the intensity variation is suppressed, which will benefit LOI extraction based on FCM. In Fig. 9(c), touching nuclei are effectively separated by the marker-controlled watershed algorithm. From the textural feature image shown in Fig. 9(d), the high- and low-density regions produce different textural energy levels. Accurate classification of the regions, however, may not result if it is only based on the textural feature. The energy-driven active contour with an appropriate stopping criterion gives satisfactory segmentation. From the results obtained with microscopic images, it can be seen that the image segmentation algorithm is effective and useful in this kind of applications.

The algorithm is a hybrid segmentation system which integrates intensity-based, edge-based and texture-based segmentation techniques. The method provides not only a closed contour corresponding to a certain object density but also density-related information in this contour. The experiment results show the effectiveness of the methodology in analysis of microscopic images.

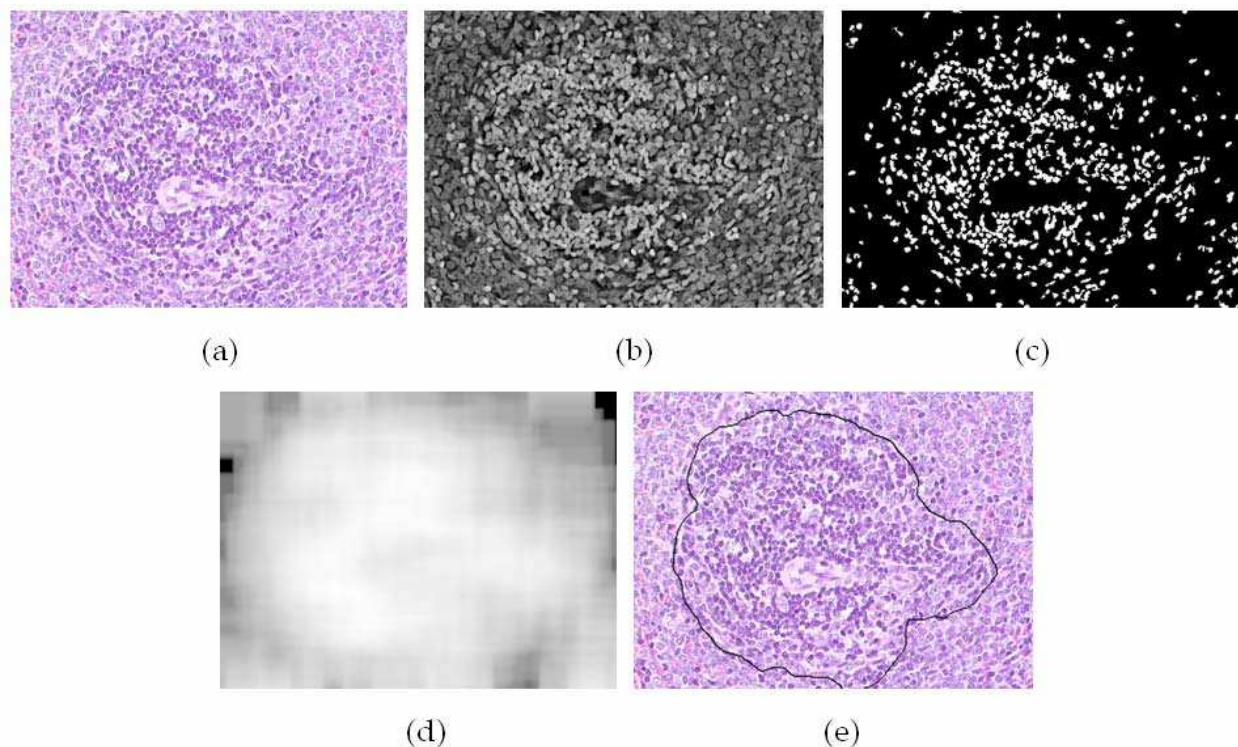


Fig. 9. Microscopic image segmentation. (a) Original image. (b) Image after preprocessing. (c) Object segmentation. (d) Textural energy map. (e) Final segmentation.

#### 4. Molecular image segmentation

The final application is about molecular marker identification in molecular images. Molecular imaging allows clinicians to visualize molecular markers and their interactions in vivo, which represents a step beyond imaging at the anatomical and functional levels. Owing to their great potential in disease diagnosis and treatment, molecular imaging techniques have undergone explosive growth over the past few decades. A method that integrates intensity and texture information under a fuzzy logic framework is developed for molecular marker segmentation (Yu & Wang, 2007).

##### 4.1 Algorithm overview

A two-dimensional fuzzy C-means (2DFCM) algorithm is used for molecular image segmentation. The most important feature of the FCM is that it allows a pixel to belong to multiple clusters according to its degree of membership in each cluster, which makes FCM-based clustering methods able to retain more information from the original image as compared to the case of crisp segmentation. FCM works well on images with low levels of noise, but has two disadvantages used in segmentation of noise-corrupted images. One is that the FCM does not incorporate the spatial information of pixels, which makes it sensitive to noise and other imaging artifacts. The other is that cluster assignment is based solely on distribution of pixel intensity, which makes it sensitive to intensity variations resulting from illumination or object geometry (Ahmed et al., 2002; Chen & Zhang, 2004; Liew et al., 2005). To improve the robustness of conventional FCM, two steps are considered in the design of the algorithm. Because the SNR of molecular images is low, image denoising is carried out

prior to segmentation. A denoising method which combines a Gaussian noise filter with an anisotropic diffusion (AD) technique is used to reduce noise in molecular images. Since the Gabor wavelet transform of molecular images is relatively robust to intensity variations, a texture characterization method based on the Gabor filter bank is used to extract texture information from images. Spatial constraints provided by denoising and texture information provided by the Gabor wavelet are embedded in the objective function of a two-dimensional fuzzy clustering (2DFCM) algorithm.

#### 4.2 Molecular image denoising

Ling and Bovik (Ling & Bovik, 2002) proposed a method to smooth molecular images by assuming an additive Gaussian model for noise. As a result, molecular images may be assumed to contain a zero-mean Gaussian white noise.

The FIR filter is well known for its ability to remove Gaussian noise from signals but it does not work very well in image processing since it blurs edges in an image. The Gaussian noise filter (GNF) (Russo, 2003) combining a nonlinear algorithm and a technique for automatic parameter tuning, is a good method for estimation and filtering of Gaussian noise. The GNF can be summarized as follows. Let  $X=\{x_1, x_2, \dots, x_n\}$  be a set of  $n$  data points in a noisy image. The output  $Y=\{y_1, y_2, \dots, y_n\}$  is defined as

$$y_i = x_i + \frac{1}{N_R} \sum_{x_r \in N_i} \zeta(x_r, x_i), \quad i = 1, \dots, n \quad (12)$$

$$\zeta(x_i, x_j) = \begin{cases} x_i - x_j & |x_i - x_j| \leq p \\ \left( \frac{3p - |x_i - x_j|}{2} \right) \text{sgn}(x_i - x_j) & p < |x_i - x_j| \leq 3p \\ 0 & |x_i - x_j| > 3p \end{cases} \quad (13)$$

where  $N_i$  stands for the neighborhood configuration with respect to a center pixel  $x_i$ ,  $N_R$  is the cardinality of  $N_i$ . The automatic tuning of parameter  $p$  is a key step in GNF. Let  $MSE(k)$  denote the mean square error between the noisy image filtered with  $p=k$  and the same image filtered with  $p=k-1$ . A heuristic estimate of the optimal parameter value is

$$\hat{p} = 2(k_m - 2) \quad (14)$$

where

$$MSE(k_m) = \text{MAX}\{MSE(k)\} \quad (15)$$

The GNF can remove intensity spikes due to the Gaussian noise, but, it has limited effect on suppressing minor intensity variations caused by the neighbourhood smoothing. Since the conventional FCM is a method based on the statistic feature of the image intensity, a piecewise-smooth intensity distribution will be greatly beneficial. More desirable denoising would result if the GNF is followed with a SRAD filter, which was introduced in Section 2.2. Suppose that the output of the SARD is represented by  $X^*=\{x_1^*, x_2^*, \dots, x_n^*\}$ . Fig. 10 shows the denoising results of GNF and SRAD.



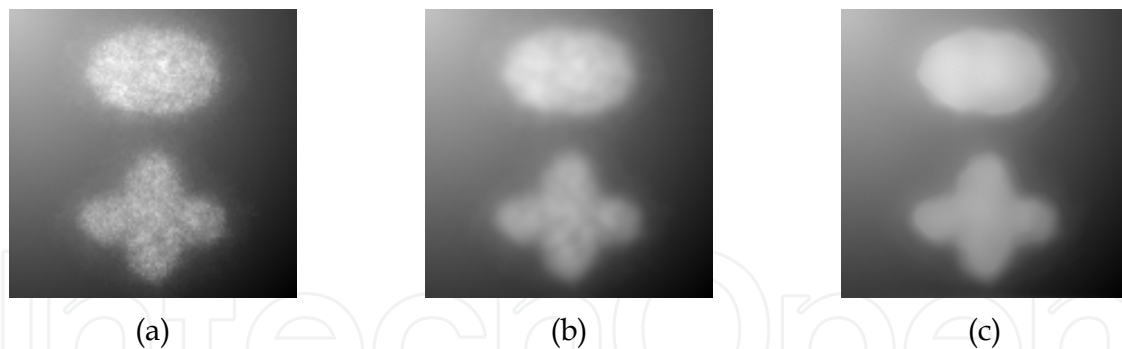


Fig. 10. Denoising by GNF and SRAD. (a) Original image. (b) After GNF filtering. (c) After GNF and SRAD filtering.

### 4.3 Texture characterization

A molecular image reveals the distribution of a certain molecule (Ling & Bovik, 2002). Since photons have different transport characteristics in different turbid tissues, a molecular image can be divided into several separate regions with each region having similar intensity (implying similar molecular concentration) and certain kind of textural pattern. Because photon distribution in a turbid tissue is usually not uniform, intensity within a region usually changes gradually. This intensity variation can cause errors when one attempts to segment images using intensity-based classification methods. Intuitively, if a feature insensitive to the slowly-varying intensity can be introduced into the classification, the image segmentation could be improved. Here a texture characterization method based on the Gabor wavelet is utilized to obtain this desirable feature.

A Gabor function in the spatial domain is a sinusoidal-modulated Gaussian function. The impulse response of the Gabor filter is given by

$$h(x, y; \mu, \theta) = \exp \left\{ -\frac{1}{2} \left[ \frac{x^2}{\sigma_x^2} + \frac{y^2}{\sigma_y^2} \right] \right\} \cdot \cos(2\pi\mu x) \quad (16)$$

where  $x = x' \cos\theta + y' \sin\theta$ ,  $y = -x' \sin\theta + y' \cos\theta$ ,  $(x, y)$  represent rotated spatial-domain rectilinear coordinates,  $u$  is the frequency of the sinusoidal wave along the direction  $\theta$  from the  $x$ -axis,  $\sigma_x$  and  $\sigma_y$  define the size of the Gaussian envelope along  $x$  and  $y$  axes respectively, which determine the bandwidth of the Gabor filter. The frequency response of the filter is given by

$$H(U, V) = 2\pi\sigma_x\sigma_y \left( \exp \left\{ -\frac{1}{2} \left[ \frac{(U-u)^2}{\sigma_u^2} + \frac{V^2}{\sigma_v^2} \right] \right\} + \exp \left\{ -\frac{1}{2} \left[ \frac{(U+u)^2}{\sigma_u^2} + \frac{V^2}{\sigma_v^2} \right] \right\} \right) \quad (17)$$

where  $\sigma_u = 1/2\pi\sigma_x$ ,  $\sigma_v = 1/2\pi\sigma_y$ . By tuning  $u$  and  $\theta$ , multiple filters that cover the spatial frequency domain can be obtained. Gabor wavelets with four different scales,  $\mu \left\{ \frac{\pi}{4\sqrt{2}}, \frac{\pi}{4}, \frac{\pi}{2\sqrt{2}}, \frac{\pi}{2} \right\}$ , and eight orientations,  $\theta \left\{ \frac{0\pi}{8}, \frac{1\pi}{8}, \dots, \frac{7\pi}{8} \right\}$  are used. Let  $X(x, y)$  be the intensity level of an image, the Gabor wavelet representation is the convolution of  $X(x, y)$  with a family of Gabor kernels; i. e.,

$$G_{\mu, \theta}(x, y) = X(x, y) * h(x, y; \mu, \theta) \quad (18)$$

where  $*$  denotes the convolution operator,  $G_{u,\theta}$  is the convolution result corresponding to the Gabor kernel at scale  $\mu$  and orientation  $\theta$ . The next step is to compute the textural energy in  $G_{u,\theta}$ . The textural energy is a measure widely used to characterize image texture. The energy that corresponds to a square window of image  $G_{u,\theta}$  centered at  $x$  and  $y$  is defined as

$$E_{\mu,\theta}(x,y) = \frac{1}{M^2} \sum_{(i,j) \in W_{xy}} |F(G_{\mu,\theta}(i,j))| \quad (19)$$

where  $M^2$  is the total number of pixels in the window, and  $F(\cdot)$  is a non-linear, sigmoid function of the form

$$F(t) = \tanh(\alpha t) = \frac{1 - e^{-2\alpha t}}{1 + e^{-2\alpha t}} \quad (20)$$

where  $\alpha$  equals to 0.25. The texture feature image is finally given by

$$T(x,y) = \frac{1}{32} \sum_{\mu,\theta} E_{\mu,\theta}(x,y) \quad (21)$$

As an example, Fig. 11(a) shows a synthetic image with intensity inhomogeneity. Fig. 11(b) shows the texture feature image. From this example, it is seen that the texture feature characterization using the Gabor wavelet is insensitive to intensity inhomogeneity.

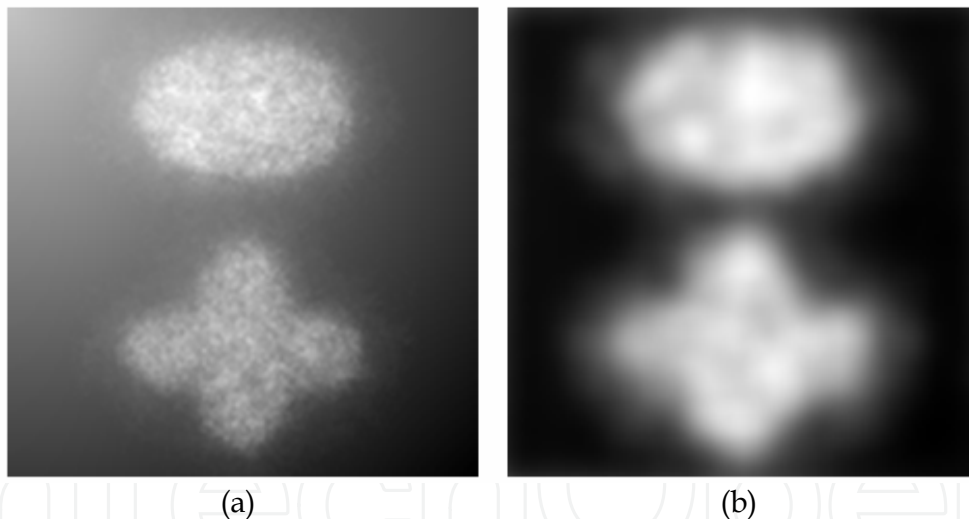


Fig. 11. Texture feature characterization. (a) Original image with intensity inhomogeneity. (b) Texture energy images for different  $u$  and  $\theta$ . (c) Texture feature image.

#### 4.4 2DFCM

The two-dimensional fuzzy C-Means (2DFCM) algorithm is constructed by integrating both the intensity and the texture information. Suppose that the denoised molecular image is  $X^* = \{x_1^*, x_2^*, \dots, x_n^*\}$  and the texture feature image is  $T = \{t_1, t_2, \dots, t_n\}$ , the objective function of 2DFCM can be expressed as

$$J_{2DFCM} = \sum_{j=1}^c \sum_{i=1}^n \mu_{ij}^b \|x_i - m_j\|^2 + \alpha \sum_{j=1}^c \sum_{i=1}^n \mu_{ij}^b \|x_i^* - m_j\|^2 + \beta_i \sum_{j=1}^c \sum_{i=1}^n \mu_{ij}^b \|t_i - v_j\|^2 \quad (22)$$

where  $\alpha$  controls the effect of denoising on clustering,  $m_j$  represents the prototype of intensity image. The influence of texture characterization on the clustering procedure can be controlled by a constant vector  $\beta_i$ , ( $i=1, \dots, n$ ), and the prototype of texture image is represented by  $v_j$ , ( $j=1, \dots, c$ ). The choice of  $\beta_i$  is based on the following principle. If  $t_i$  is large, implying dominant textural energy,  $\beta_i$  should be large; if  $t_i$  is small,  $\beta_i$  should be also small.  $\beta_i$  is determined by  $\beta_i = (Bt_i) / \max(T)$ . Both  $\alpha$  and  $B$  are determined by trial-and-error.

The optimization problem under constraint  $U$  in (5) can be solved by using a Lagrange multiplier  $\lambda$  in the following functional,

$$F = \sum_{j=1}^c \sum_{i=1}^n \mu_{ij}^b \|x_i - m_j\|^2 + \alpha \sum_{j=1}^c \sum_{i=1}^n \mu_{ij}^b \|x_i^* - m_j\|^2 + \beta_i \sum_{j=1}^c \sum_{i=1}^n \mu_{ij}^b \|t_i - v_j\|^2 + \lambda \left( 1 - \sum_{j=1}^c \mu_{ij} \right) \quad (23)$$

Taking the derivative of  $F$  with respect to  $\mu_{ij}$  and setting the result to zero, we can obtain an equation for  $\mu_{ij}$  with  $\lambda$  unknown

$$\mu_{ij} = \left\{ \frac{\lambda}{b[(x_i - m_j)^2 + \alpha(x_i^* - m_j)^2 + \beta_i(t_i - v_j)^2]} \right\}^{\frac{1}{(b-1)}} \quad (24)$$

Utilize constraint  $U$ ,  $\lambda$  can be solved as

$$\lambda = \left\{ \sum_{k=1}^c \left\{ b[(x_i - m_k)^2 + \alpha(x_i^* - m_k)^2 + \beta_i(t_i - v_k)^2] \right\}^{\frac{1}{(b-1)}} \right\}^{b-1} \quad (25)$$

By substituting (25) into (24), a necessary condition for (22) to be at a local minimum will be obtained as

$$\mu_{ij} = \frac{\left[ (x_i - m_j)^2 + \alpha(x_i^* - m_j)^2 + \beta_i(t_i - v_j)^2 \right]^{\frac{1}{(b-1)}}}{\sum_{k=1}^c \left[ (x_i - m_k)^2 + \alpha(x_i^* - m_k)^2 + \beta_i(t_i - v_k)^2 \right]^{\frac{1}{(b-1)}}} \quad (26)$$

Similarly, by zeroing the derivatives of  $F$  with respect to  $m_j$  and  $v_j$ , we have

$$m_j = \frac{\sum_{i=1}^n \mu_{ij}^b (x_i + \alpha x_i^*)}{(1 + \alpha) \sum_{i=1}^n \mu_{ij}^b}, \quad v_j = \frac{\sum_{i=1}^n \mu_{ij}^b t_i}{\sum_{i=1}^n \mu_{ij}^b} \quad (27)$$

The procedure of 2DFCM can be summarized in the following steps:

1. Filter the image by GNF followed by SRAD to generate the denoised image  $X^*$ ;
2. Filter the image by Gabor wavelet band and compute the texture feature image  $T$ ;
3. Formulate the 2D histogram with the denoised image  $X^*$  and the texture feature image  $T$ ; Estimate the number of clusters ( $c$ ) and initial prototypes ( $M$ ), and
4. Repeat following steps until the centroid variation is less than 0.001:

- a. Update the membership function matrix with (26).
- b. Update the centroids with (27).
- c. Calculate the centroid variation and before and after updating.

#### 4.5 Algorithm performance

The performance of the 2DFCM is first tested with simulated molecular images, from which the ground truth is available. Simulated molecular images are obtained by using MOSE (Monte Carlo optical simulation environment) (Li et al., 2004; Li et al., 2005) developed by the Bioluminescence Tomography Lab, Departments of Radiology & Departments of Biomedical Engineering, University of Iowa (<http://radiology.uiowa.edu/>). MOSE is based on the Monte Carlo method to simulate bioluminescent phenomena in the mouse imaging and to predict bioluminescent signals around the mouse.

The optimized  $\alpha$  and  $B$  in the 2DFCM should be obtained by trial-and-error.  $\alpha=3.5$  and  $B=36$  are used. The computation time of the algorithm for an image of  $128 \times 128$  is approximately 12 seconds on a personal computer. About two-thirds of the time is consumed in texture characterization based on Gabor wavelet. The first example is for applying the algorithm to a synthetic cellular image and comparing the 2DFCM with FCM. The synthetic image is shown in Fig. 12(a). The segmentation results by 2DFCM and FCM are presented in Figs. 12(b) and (c), respectively.

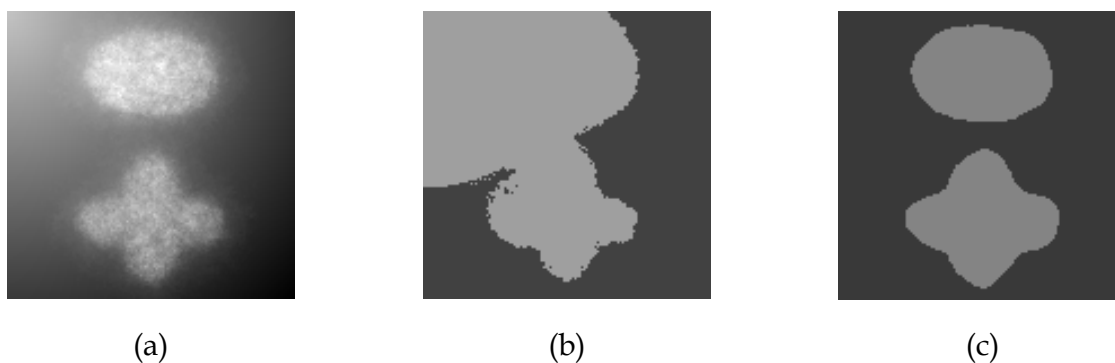


Fig. 12. Segmentation results on the first synthetic image. (a) The synthetic image generated by MOSE. (b) Segmentation by FCM. (c) Segmentation by 2DFCM.

In the second example, the algorithm is applied to a real molecular image ( $256 \times 256$ ) (as shown in Fig. 13(a)). Figs. 13(b) and (c) show the denoising result by the GNF plus SRAD, and the texture feature image obtained by the Gabor wavelet bank, respectively. Figs. 13(d) and (f) show the segmentation results of by FCM and 2DFCM, respectively. In order to illustrate the segmentation results clearly, the contours of the region of interest in the classification image are extracted and superimposed on the original image. Figs. 13(e) and (g) give the contour comparisons.

From the experimental results, we can see that denoising by GNF plus SRAD are satisfactory. The Gabor wavelet bank can represent the texture information in the molecular image without disturbance by intensity variation. Intensity inhomogeneity degenerates segmentation by the FCM. Since the 2DFCM utilizes both the intensity and texture information simultaneously, it produces more satisfactory results than the FCM.

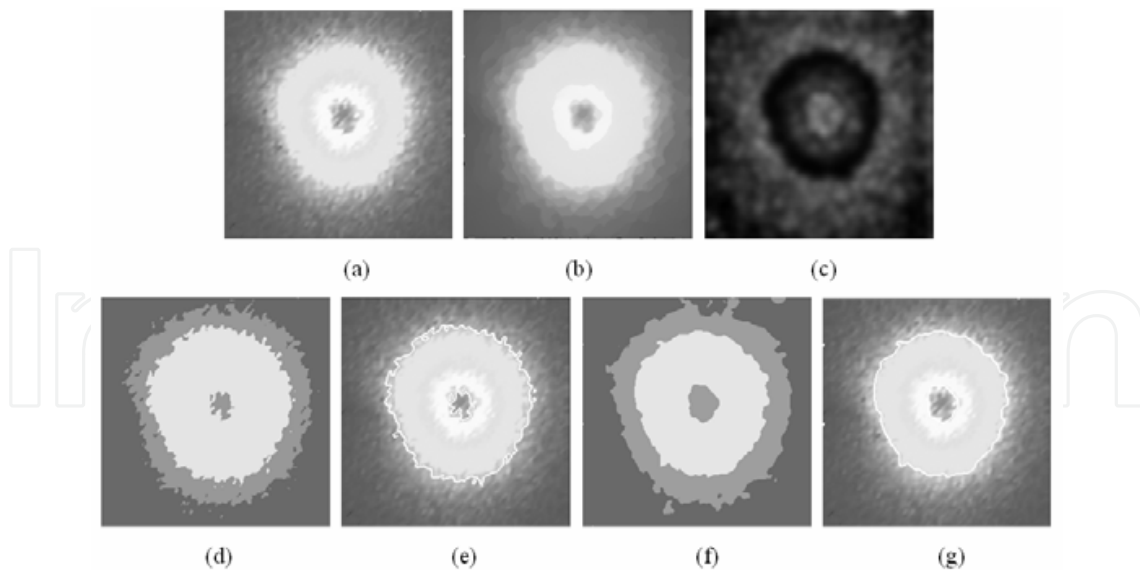


Fig. 13. Segmentation results for a real molecular image. (a) Original image. (b) Denoising result by GNF plus SRAD. (c) Texture feature image. (d) Segmentation result by FCM. (e) Contour obtained from (d) superimposed on the original image. (f) Segmentation result by 2DFCM. (g) Contour obtained from (f) superimposed on the original image.

## 5. Conclusion

In this chapter, segmentation of three different kinds of biomedical images is discussed. Biomedical images obtained from different modalities suffer from different imaging noises. Image segmentation techniques based on only one image feature usually fail to produce satisfactory segmentation results for biomedical images. Three methodologies are presented for the segmentation of ultrasound images, microscopic images and molecular images, respectively. All these segmentation methodologies integrate image features generated from image intensity, edges and texture to reduce the effect of noises on image segmentation. It can be concluded that a successful medical image segmentation method needs to make a use of varied image features and information in an image.

## 6. References

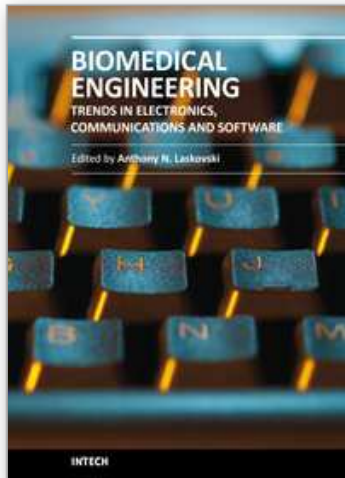
- Ahmed, M.N.; Yamany, S.M.; Mohamed, N.; Farag, A.A. & Moriarty, T. (2002). A modified fuzzy c-means algorithm for bias field estimation and segmentation of MRI data. *IEEE Trans. Med Imag.*, Vol. 21, No. 3, (March 2002) (193-199), ISSN: 0278-0062
- Bezdek, J.C. (1981). A convergence theorem for the fuzzy ISODATA clustering algorithm. *IEEE Trans. Pattern Anal. Mach. Intell.*, Vol. 2, No. 1, (January 1980) (1-8), ISSN: 0162-8828
- Bezdek, J.C. (1981). *Pattern Recognition with Fuzzy Objective Function Algorithms*, Kluwer Academic Publishers, ISBN: 0306406713, Norwell, MA, USA
- Canny, J.F. (1986). A computational approach to edge detection. *IEEE Trans. Pattern Anal. Mach. Intell.*, Vol. 8, No. 6, (November 1986) (679-698), ISSN: 0162-8828
- Chan, T.F. & Vese, L.A. (2001). Active contours without edges, *IEEE Trans. Image Process.*, Vol. 10, No. 2, (February 2001) (266-277), ISSN: 1057-7149



- Chaudhuri, B.B. & Sarkar, N. (1995). Texture segmentation using fractal dimension. *IEEE Trans. Pattern Anal. Mach. Intell.*, Vol. 17, No. 1, (January 1995) (72-76), ISSN: 0162-8828
- Chen, S. & Zhang, D. (2004). Robust image segmentation using FCM with spatial constraints based on new kernel-induced distance measure. *IEEE Trans. Syst., Man, Cybern.*, Vol. 34, No.4, (April 2004) (1907-1916), ISSN: 0018-9472
- FjØrtoft R., Lopés A., Marthon P. & Cubero-Castan E. (1998). An optimal multiedge detector for SAR image segmentation. *IEEE Trans Geosci Remote Sensing*, Vol. 36, No. 3, (May 1998) (793-802), ISSN: 0196-2892
- Haris, K.; Efstratiadis, S.N.; Maglaveras, N. & Katsaggelos, A.K. (1998). Hybrid image segmentation using watersheds and fast region merging. *IEEE Trans. Image Process.*, Vol. 7, No. 12, (December 1998) (1684-1699), ISSN: 1057-7149
- Haralick R. (1982). Zero crossing of second directional derivative edge operator. *Proceedings of SPIE Symp Robot Vision*, pp. 91-99, Washington, DC, May 1982.
- Hsiao, J.Y. & Sawchuk, A.A. (1989). Supervised texture image segmentation using feature smoothing and probabilistic relaxation techniques. *IEEE Trans. Pattern Anal. Mach. Intell.*, Vol. 11, No. 12, (December 1989) (1279-1292), ISSN: 0162-8828
- Jackway, P. (1996). Gradient watersheds in morphological scale-space. *IEEE Trans. Image Process.*, Vol. 5, No. 6, (June 1996) (913-921), ISSN: 1057-7149
- Jain, A.K. & Farrokhnia, F. (1991). Unsupervised texture segmentation using Gabor filters. *Pattern Recognition*, Vol. 24, No. 12 (December 1991) (1167-1186), ISSN: 0031-3203
- Li, H.; Tian, J.; Cong, W.X.; Wang, L.V.; Hoffman, E.A. & Wang G. (2004). A mouse optical simulation environment (MOSE) to investigate bioluminescent phenomena in the living mouse with Monte Carlo method. *Academic Radiology*, vol. 11, no. 9, (September 2004) (1029-1038), ISSN: 1076-6332
- Li, H.; Tian, J.; Luo, J.; Wang, G. & Cong, W.X. (2005). Interactive graphic editing tools in bioluminescent imaging simulation. *BioOptics of SPIE 2005*, pp. 22-24, San Diego, Jan. 2005. California USA.
- Liew, A.W.C.; Yan, H. & Law, N.F. (2005). Image segmentation based on adaptive cluster prototype estimation. *IEEE Trans. Fuzzy Syst.*, Vol. 13, No. 4, (August 2005) (444-453), ISSN: 1063-6706
- Ling, J. & Bovik, A.C. (2002). Smoothing low-SNR molecular images via anisotropic mediana-diffusion. *IEEE Trans. Med Imag.*, Vol. 21, No. 4, (April 2002) (377-384), ISSN: 0278-0062
- Kass, M.; Witkin, A. & Terzopoulos, D. (1988). Snakes: active contour models. *Int. J. Comput. Vis.*, Vo. 1, No. 4, (January 1988) (321-331), ISSN: 0920-5691
- Larson, G.W.; Rushmeier, H. & Piatko, C. (1997). A visibility matching tone reproduction operator for high dynamic range scenes. *IEEE Trans. Vis. Comput. Gr.*, Vol. 3, No. 4, (October-December 1997) (291-306), ISSN: 1077-2626
- Lu, W.; Tan, J. & Floyd, R. (2005). Automated fetal head detection and measurement in ultrasound images by iterative randomized Hough transform. *Ultrasound Med Biol.*, Vol. 31, No. 7, (July 2005) (929-936), ISSN: 0301-5629
- Mandelbrot, B.B. (1976). How long is the coast of Britain? Statistical self-similarity and fractal dimension. *Science*, Vol. 156, No. 37, (May 1967) (636-638), ISSN: 0036-8075
- Otsu, N. (1979). A threshold selection method from gray-level histograms. *IEEE Trans. Syst., Man, Cybern.*, Vol. 9, No. 1, (January 1979) (62-66), ISSN: 0018-9472



- Pappas, T.N. (1992). An adaptive clustering algorithm for image segmentation, *IEEE Trans. Signal Process.*, Vol. 40, No. 4, (April 1992) (901-914), ISSN: 1053-587X
- Pentland, A.P. (1984). Fractal based description of natural scenes, *IEEE Trans. Pattern Anal. Mach. Intell.*, Vol. 6, No. 6, (November 1984) (661-674), ISSN: 0162-8828
- Randen, T. & Husoy, J.H. (1999). Filtering for texture classification: a comparative study. *IEEE Trans. Pattern Anal. Mach. Intell.*, Vol. 21, No. 4, (April 1999) (291-310), ISSN: 0162-8828
- Russo, F. (2003). A method for estimation and filtering of Gaussian noise in images. *IEEE Trans. Instrum. & Meas.*, Vol. 52, No. 4, (August 2003) (1148-1154), ISSN: 0018-9456
- Sahoo, P.K.; Soltani, S.; Wong, A.K.C. & Chen, Y.C. (1988). A survey of thresholding techniques. *Comput. Vis. Graph. Image Process.*, Vol. 41, No. 2, (February 1988) (233-260), ISSN: 0734-189X
- Tyagi, A. & Bayoumi, M.A. (1992). Image segmentation on a 2-D array by a directed split and merge procedure. *IEEE Trans. Signal Process.*, Vol. 40, No. 11, (November 1992) (2804-2813), ISSN: 1053-587X
- Vincent, L. (1993). Morphological grayscale reconstruction in image analysis: application and efficient algorithm. *IEEE Trans. Image Process.*, Vol. 2, No. 2, (April 1993) (176-201), ISSN: 1057-7149
- Vincent, L. & Soille, P. (1991). Watersheds in digital spaces: an efficient algorithm based on immersion simulations, *IEEE Trans. Pattern Anal. Mach. Intell.*, Vol. 13, No. 6, (June 1991) (583-598), ISSN: 0162-8828
- Wu, X. (1993). Adaptive split-and-merge segmentation based on piecewise least-square approximation. *IEEE Trans. Pattern Anal. Mach. Intell.*, Vol. 15, No. 8, (August 1993) (808-815), ISSN: 0162-8828
- Xu, C. & Prince, J.L. (1998). Snakes, shapes, and gradient vector flow, *IEEE Trans. Image Process.*, Vol. 7, No. 3, (March 1998) (359-369), ISSN: 1057-7149
- Yang, X.; Li, H. & Zhou, X. (2006). Nuclei segmentation using marker-controlled watershed, tacking using mean-shift, and Kalman filter in time-lapse microscopy. *IEEE Trans. Circuits and Systems*, Vol. 53, No.11, (November 2006) (2405-2414), ISSN: 1057-7122
- Yu, J. & Wang, Y. (2007). Molecular image segmentation based on improved fuzzy clustering. *Int. J. Bio. Imag.*, Vol. 2007, (July 2007) (1-9), ISSN: 1687-4188
- Yu, J.; Wang, Y.; Chen, P. & Shen, Y. (2008a). Fetal abdominal contour extraction and measurement in ultrasound images. *Ultrasound Med Biol.*, Vol. 34, No. 2, (February 2008) (169-182), ISSN: 0301-5629
- Yu, J.; Wang, Y. & Chen, P. (2008b). Fetal ultrasound image segmentation system and its use in fetal weight estimation. *Med. Biol. Eng. Comput.*, Vol. 46, No. 12, (December 2008) (1227-1237), ISSN: 0140-0118
- Yu, J. & Tan, J. (2009). Object density-based image segmentation and its applications in biomedical image analysis. *Comput. Meth. Prog. Bio.*, Vol. 96, No. 3, (December 2009) (193-204), ISSN: 0169-2607
- Yu Y. & Acton S.T. (2002). Speckle reducing anisotropic diffusion. *IEEE Trans Image Process*, Vol. 11, No. 11, (November 2002) (1260-1270), ISSN: 1057-7149
- Yu Y. & Acton S.T. (2004). Edge detection in ultrasound imagery using the instantaneous coefficient of variation. *IEEE Trans Image Process*, Vol. 13, No. 12, (December 2004) (1640-1655), ISSN: 1057-7149
- Zucker, S. & Terzopoulos, D. (1980). Finding structure in co-occurrence matrices for texture analysis. *Comput. Graph. Image Process.*, Vol. 12, No. 3, (March 1980) (286-308), ISSN: 0146-664X



## **Biomedical Engineering, Trends in Electronics, Communications and Software**

Edited by Mr Anthony Laskovski

ISBN 978-953-307-475-7

Hard cover, 736 pages

**Publisher** InTech

**Published online** 08, January, 2011

**Published in print edition** January, 2011

Rapid technological developments in the last century have brought the field of biomedical engineering into a totally new realm. Breakthroughs in materials science, imaging, electronics and, more recently, the information age have improved our understanding of the human body. As a result, the field of biomedical engineering is thriving, with innovations that aim to improve the quality and reduce the cost of medical care. This book is the first in a series of three that will present recent trends in biomedical engineering, with a particular focus on applications in electronics and communications. More specifically: wireless monitoring, sensors, medical imaging and the management of medical information are covered, among other subjects.

### **How to reference**

In order to correctly reference this scholarly work, feel free to copy and paste the following:

Jinhua Yu, Jinglu Tan and Yuanyuan Wang (2011). Biomedical Image Segmentation Based on Multiple Image Features, Biomedical Engineering, Trends in Electronics, Communications and Software, Mr Anthony Laskovski (Ed.), ISBN: 978-953-307-475-7, InTech, Available from:  
<http://www.intechopen.com/books/biomedical-engineering-trends-in-electronics-communications-and-software/biomedical-image-segmentation-based-on-multiple-image-features>

**INTECH**  
open science | open minds

### **InTech Europe**

University Campus STeP Ri  
Slavka Krautzeka 83/A  
51000 Rijeka, Croatia  
Phone: +385 (51) 770 447  
Fax: +385 (51) 686 166  
[www.intechopen.com](http://www.intechopen.com)

### **InTech China**

Unit 405, Office Block, Hotel Equatorial Shanghai  
No.65, Yan An Road (West), Shanghai, 200040, China  
中国上海市延安西路65号上海国际贵都大饭店办公楼405单元  
Phone: +86-21-62489820  
Fax: +86-21-62489821

© 2011 The Author(s). Licensee IntechOpen. This chapter is distributed under the terms of the [Creative Commons Attribution-NonCommercial-ShareAlike-3.0 License](https://creativecommons.org/licenses/by-nc-sa/3.0/), which permits use, distribution and reproduction for non-commercial purposes, provided the original is properly cited and derivative works building on this content are distributed under the same license.

IntechOpen

IntechOpen